Title

Optimized, Omnidirectional Surface Acoustic Wave Source: 152° Y-Rotated Cut of Lithium Niobate for Acoustofluidics

Journal

IEEE Transactions on Ultrasonics Ferroelectrics and Frequency Control, 67(10)

ISSN

0885-3010

Authors

Zhang, Naiqing
Mei, Jiyang
Gopesh, Tilvawala
et al.

Publication Date

2020-10-01

DOI

10.1109/tuffc.2020.2993766

Peer reviewed

Optimized, omnidirectional surface acoustic wave source: 152 degree Y-rotated cut of lithium niobate for acoustofluidics

Naiqing Zhang, Jiyang Mei, *Member, IEEE,* Tilvawala Gopesh, and James Friend, *Fellow, IEEE*

***Abstract*—Here we propose an optimized Y-rotated cut of LN for multi-directional surface acoustic wave propagation, simultaneously minimizing the anisotropic effects while maximizing the electromechanical properties of this cut of LN. The goal is to offer a piezoelectric material suitable for acoustofluidics applications that require greater flexibility in wave generation and propagation than the currently ubiquitous 128-degree Y-rotated X-propagating cut. The 128YX LN cut is known to most effectively generate Rayleigh SAW along the X direction alone. Any SAW veering from this propagation direction is affected by beam steering and changes in resonance frequency and electromechanical coupling coefficients, consequently limiting the use of LN in various acoustofluidics applications where more diverse configurations would be beneficial.**

The $\mathcal{L}_2$-norm of these properties was evaluated under rotational transformation to produce a physical model with closed governing equations for 40 MHz surface wave propagation on the surface of a piezoelectric material. This was then utilized to obtain the surface wave velocity and coupling coefficient of the specific Y-cut LN with respect to the propagating direction. Next, the averaged coupling coefficients of various Y-cuts of LN in all propagating directions were calculated and integrated to simultaneously minimize anisotropy and maximize the electromechanical properties of the LN substrate. A 152-deg. Y-rotated cut was found to be the optimal choice under these constraints, enabling multi-directional surface acoustic wave propagation with greater coupling and lower variation in wave performance for SAW generated across the surface in any direction. Compared to the 128YX LN cut, this cut provides a 66.5% improvement in the in-plane isotropy and a 37.0% improvement in the average electromechanical coupling for in-plane SAW propagation. Experimental devices operating at the frequency of 40 MHz were designed, fabricated, and tested on the surface of this 500 μm-thick specific cut of LN and served to verify the supporting analysis and the superior isotropic properties of the 152-deg. Y-rotated cut in generating SAW.

***Index Terms*—isotropic, coupling coefficient, optimized cut, lithium niobate, surface acoustic wave propagation.**

I. Introduction

COMPARED to traditional forms of ultrasound used over the years in manipulating solids and fluids as physical acoustics phenomena, surface acoustic waves are relatively high-frequency (10 MHz to 1 GHz) acoustic waves that offer accelerations in excess of 10^8 m/s^2 at wavelengths commensurate with the dimensions of micro to nano-scale fluidic structures, as comprehensively described by Friend and Yeo [1]. Termed *acoustofluidics*, the combination of physical acoustics and the use of surface acoustic waves and other, related high frequency waves is producing a diverse range of solutions to long-standing problems in fluid and particle manipulation in lab, organ, and organism-on-a-chip technologies for medicine and biology as described in recent review contributions [2, 3]. Despite the many limitations in generating, controlling, and propagating surface acoustic waves (SAW) within lithium niobate (LN) substrates, there is now consistent evidence of the remarkable promise of SAW in controlling fluid and particle behavior [4, 5]. Lithium niobate is ubiquitous in SAW generation and propagation due to its large coupling coefficient relative to other single crystalline materials for SAW (and other waveforms [6]), absence of hysteresis and heating common in polycrystalline piezoelectric materials [7], and outright convenience in comparison to ZnO, AlN, and other thin-film piezoelectric materials.

In 1976, Shibayama *et al.* [8] found the 127.86° Y-rotated cut to be optimal for generating Rayleigh SAW along a single axis, even though the 131° Y-rotated cut had previously demonstrated [9] the highest electromechanical coupling coefficient and lowest insertion loss. The 127.86° cut reduced the generation of parasitic bulk waves compared to the 131° cut, and the 127.86° Y-rotated, X-propagating cut of LN (128YX LN) has since become the most popular and widely accepted orientation for applications requiring Rayleigh SAW waves. However, the 128YX cut efficiently generates SAW only along the X direction, ideal for telecommunications but a problem in acoustofluidics where the ability to change the wave propagation direction to go around obstacles, deflect into features, and produce two-dimensional acoustic wave structures in a piezoelectric substrate would be beneficial. Any SAW generated at an angle to the X-axis propagation direction encounters beam steering and a reduction in electromechanical coupling, an issue known for many years in microrobotic [10] and acoustofluidic applications. Worse, since the SAW propagation velocity also changes, either the frequency must change to deliver a SAW of the same wavelength or the generating electrodes' dimensions must be carefully tailored to deliver SAW at a constant frequency. With similarly sized electrodes and driving conditions upon 128YX LN, the vibration displacement and particle velocity of a SAW along the X-axis are *double* these values for SAW along the Y-axis [11] due to the significant difference in electromechanical coupling along these propagation directions.

All authors are with the Medically Advanced Devices Laboratory, Center for Medical Devices, Department of Aerospace Engineering, Jacobs School of Engineering, and the Department of Surgery, School of Medicine, University of California San Diego, 9500 Gilman Drive, La Jolla, CA 92093 USA e-mail: jfriend@ucsd.edu web: http://friend.ucsd.edu

Determining how acoustic waves propagate on the surface of anisotropic, piezoelectric materials is a classic topic. Representing the acoustic waves as a linear, small amplitude—1% strain or less—phenomenon produces a complicated set of partial differential equations that, with work [12, 13], produces transcendental equations that are rarely solvable in closed form [14]. In some crystal symmetries, such as the x_3 plane of a monoclinic crystal, on a half space of an incompressible monoclinic material, or along a material axis of a rhombohedral material, explicit secular equations can be produced and solved to produce predictions for surface acoustic wave velocities [15]. But in anisotropic materials in a more general sense, the classic partial waves-based approach first defined by Farnell [16] is an effective numerically-based route to determining a surface acoustic wave's propagation velocities, modes, and other characteristics. We adopt this approach, further investigating the surface impedance matrices to verify both the existence and velocities of SAW upon anisotropic media [13, 14, 17, 18]. Recently, rather complex arrangements for wave propagation have been considered, including multilayer structures [19, 20], strip waveguides [21, 22], air-gapped devices [23], interface-guiding structures [24], and fluid coupling [25], and these could be considered to be extensions of the classic methods to very specific wave propagation applications.

Here we consider a simpler route, exploring rotated cuts of single crystal LN that may better suit acoustofluidics applications. Our aim is to obtain an optimized piezoelectric material orientation by utilizing well-established theoretical models that would not only be compatible with all previous numerical analyses to obtain specific wave characteristics, but would also be better suited for acoustofluidics and lab-on-a-chip applications where SAW propagation along other axes beside the X axis would be beneficial.

An alternative might be to employ thin-film, deposited piezoelectric polycrystalline ceramic materials such as ZnO or AlN, on a silicon or similar solid substrate [26, 27] to offer isotropic in-plane behavior. These thin films offer flexibility in electrode designs, wave generation and propagation, and other features [28] potentially useful in acoustofluidics. For example, isotropic SAW has been generated on ZnO thin films to produce a needle-shape liquid column on a free liquid surface [29, 30, 31, 32]. However, these materials possess low electro-mechanical coupling coefficients in comparison to LN, and are unable to generate large power transmission from electrical to mechanical domains commensurate with typical acoustofluidics applications due to their clamped, thin-film configuration, and require additional steps in ultraviolet lithography. Therefore, a cut of a single crystal bulk material that has, simultaneously, a reduced in-plane anisotropy and increased electromechanical coupling coefficient would be superior.

Here, we propose a Y-rotated cut of LN optimized for multi-directional SAW propagation, simultaneously minimizing in-plane anisotropy and maximizing in-plane electromechanical coupling for acoustofluidic applications. Rotational transformation of the material properties of LN is performed to produce an $\mathcal{L}_2$-norm-based comparison to isotropic material properties to find the LN cut with the least anisotropic in-plane properties, that is, the closest to isotropic properties possible along the surface plane of the substrate. A physical model with closed governing equations for surface wave propagation on the LN is then used to determine the open and short-circuit surface wave velocity and, consequently, the electromechanical coupling coefficient along any direction on the substrate. The coupling coefficients of a given Y-cut of LN for SAW propagating in all planar directions are then calculated. These results are combined with the results of the in-plane anisotropy analysis to collectively identify a Y-rotated cut of LN that offers the best ability to generate and propagate SAW in an arbitrary direction upon the LN substrate, minimizing planar anisotropy and maximizing planar SAW electromechanical properties. This process produced the 152° Y-axis rotated cut of LN, upon which SAW devices were designed, fabricated, and tested to verify the outcomes of the analysis. In particular, we were able to verify the ability to generate and propagate SAW in directions beyond the standard X-axis of 128YX LN. We offer a consistent method for tailoring the selection of the cut to fit desired design goals. This is essential for the development of acoustofluidic devices based on SAW and would be relevant in numerous other acoustic devices that rely on IDTs or arrays of multiple transducers [33, 34, 35, 36].

II. Determination of the "least" in-plane anisotropic Y-rotated cut of LN

Since the stiffness tensor underpins the mechanical elastic properties of a material and determines its wave propagation and generation modes and its electro-mechanical properties, we consider how rotational transformation of the LN stiffness tensor affects its apparent anisotropy in comparison with isotropic materials. For those unaware, isotropic materials are inherently unable to offer piezoelectricity, and our aim here is instead to minimize the anisotropy in the surface plane of the LN upon which the SAW will be generated and propagated. While X-axis or X and Y rotated cuts could be considered in a more general exploration using the methods we propose, obtaining such cuts is a practical problem: LN producers do not offer such flexibility in the material orientation nor are set up to do so for research-relevant quantities of wafers.

A. Rotational transformation of the stiffness tensor

We consider a variety of Y-rotated LN cuts with a focus on offering the least anisotropic response along the 360° of the plane as opposed to solely the greatest coupling for a particular Rayleigh-SAW propagation direction. The latter has previously been studied and initially resulted in the 131° Y-rotated cut and soon after the 127.86° Y-rotated cut. We later consider the electromechanical coupling, but first describe the rotational transformation that produces the so-called *Y-rotated cut* of LN, as shown in Fig. 1(a). The coordinate system $Oxyz$ is composed of the original principal axes of the single crystal LN. The coordinate system $Ox'y'z'$ defines the LN substrate surface plane due to a rotation θ about the x axis as shown in Fig. 1(a): the x and x' axes are coincident, the x and y' axes are in the plane of the substrate, and z' is perpendicular

to the substrate. The standard name of such a cut of LN is the $\theta + 90^\circ$ Y-rotated cut, illustrated at right in Fig. 1(a). In other words, the standard 127.86° Y-rotated cut would produce a rotation angle of $\theta = 37.86^\circ$ here.

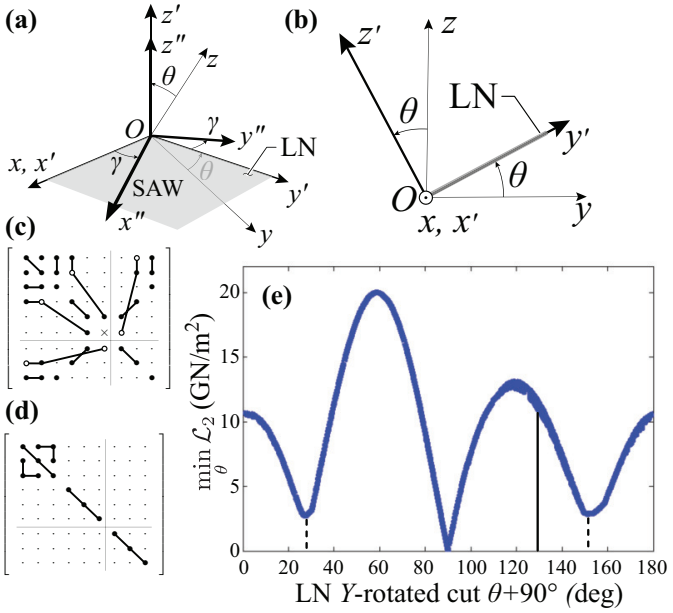

Fig. 1: The rotation from the LN material's principal axes in coordinate system $Oxyz$ to the desired substrate orientation defined by coordinate system $Ox'y'z'$ may either be viewed from the perspective of the (a) substrate in plane $x'Oy'$ or (b) the LN material's principal axes in coordinate system $Oxyz$. The "cut angle" is traditionally defined as $\theta + 90^\circ$, here the total angle between the y and z' axes. The SAW is presumed to (a) propagate along axis x'' upon the substrate surface plane $x'Oy'$ at an angle γ from the positive x' axis. The coordinate system $Ox''y''z''$ is dedicated to SAW propagation. A standard illustration of the symmetry present in a (c) trigonal $3m$ media such as LN is provided alongside a similar representation for an (d) isotropic media, indicating the material-defined elastic, piezoelectric, and dielectric tensor properties in shortened Voigt form, enabling the representation of the associated tensors by matrices with details in the Appendix. (e) The minimum $\mathcal{L}_2$-norm plotted with respect to the cut angle $\theta + 90^\circ$ for LN indicates three minima: the well-known Z cut, a purely isotropic response at $\theta = 0^\circ$, alongside the $\theta = 62^\circ$ and $\theta = 118^\circ$ values. The latter two represent the 152° and 28° Y-rotated cuts, respectively. Dashed lines indicate these two cuts alongside a solid line indicating the standard 128° cut, illustrating the ability to improve overall isotropy in the $Ox'y'z'$ by choosing other cuts beside the 128° Y-rotated cut.

We first note the relationship between the original and the rotated coordinate systems' unit vectors as

$$\begin{pmatrix}\mathbf{e}_1\\ \mathbf{e}_2\\ \mathbf{e}_3\end{pmatrix} = \begin{pmatrix}1 & 0 & 0\\ 0 & \cos\theta & -\sin\theta\\ 0 & \sin\theta & \cos\theta\end{pmatrix}\begin{pmatrix}\mathbf{e}'_1\\ \mathbf{e}'_2\\ \mathbf{e}'_3\end{pmatrix} = [A]\begin{pmatrix}\mathbf{e}'_1\\ \mathbf{e}'_2\\ \mathbf{e}'_3\end{pmatrix}, \quad (1)$$

with the Euler transformation matrix $[A]$ defined as shown. In component notation ($m, n \in \{1, 2, 3\}$) , the equation may be written as

$$\mathbf{e}_m = A_{mn}\mathbf{e}'_n. \quad (2)$$

Expressing the stiffness tensor c^E_{ijkl} in component notation ($i, j, k, l \in \{1, 2, 3\}$) and enforcing the Einsteinian summation convention [12] with superscript E referring to a constant electric field, we may write the following for these two different coordinate systems by using eqn. (2):

$$\begin{aligned} c^{E\prime}_{pqrs}\mathbf{e}'_p\mathbf{e}'_q\mathbf{e}'_r\mathbf{e}'_s &= c^E_{ijkl}\mathbf{e}_i\mathbf{e}_j\mathbf{e}_k\mathbf{e}_l \\ &= c^E_{ijkl}A_{ip}A_{jq}A_{kr}A_{ls}\mathbf{e}'_p\mathbf{e}'_q\mathbf{e}'_r\mathbf{e}'_s. \end{aligned} \quad (3)$$

Details of the notation are provided for the reader's convenience in the Appendix. A rotational transformation from the original stiffness tensor dependent solely on θ to produce the transformed stiffness tensor $c^{E\prime}_{pqrs}$ may then be written as

$$c^{E\prime}_{pqrs} = c^E_{ijkl}A_{ip}A_{jq}A_{kr}A_{ls}. \quad (4)$$

B. Identifying the Least Anisotropic In-plane Y-cut of LN by Norm Comparison with Isotropic In-plane Materials

To investigate the extent of *planar* anisotropy in the plane $x'Oy'$ of θ-rotated LN, a double inner product between the unit vector $\mathbf{e}'_3$ normal to the substrate surface and the stiffness tensor in the rotated coordinate system shown in eqn. (3) may be taken:

$$\mathbf{e}'_3 \cdot (c^{E\prime}_{pqrs}\mathbf{e}'_p\mathbf{e}'_q\mathbf{e}'_r\mathbf{e}'_s) \cdot \mathbf{e}'_3 = c^{E\prime}_{3qr3}\mathbf{e}'_q\mathbf{e}'_r. \quad (5)$$

To determine which orientation of LN produces the most isotropic in-plane properties, we then consider the stiffness tensor for an isotropic material. It is well-known that isotropic materials cannot be piezoelectric as at least asymmetry through a reflection (for example, Hermann-Mauguin group ∞mm) is necessary, but this aspect is treated later via the electromechanical coupling. Noting the symmetry of the trigonal ($3m$) LN's intrinsic mechanical, piezoelectric, and electrical properties (*see* Appendix A for the definition and representations of the corresponding tensors) in Fig. 1(c) versus isotropic media in Fig. 1(d), it becomes apparent what quantities that describe the LN's stiffness must be changed to become more isotropic. Subsequently, the same operations were performed on the stiffness tensor for the isotropic material as the trigonal LN. We begin with the double inner product to determine the expression for the stiffness along the plane $x'Oy'$,

$$\mathbf{e}'_3 \cdot (c^{\text{iso}}_{pqrs}\mathbf{e}'_p\mathbf{e}'_q\mathbf{e}'_r\mathbf{e}'_s) \cdot \mathbf{e}'_3 = c^{\text{iso}}_{3qr3}\mathbf{e}'_q\mathbf{e}'_r, \quad (6)$$

where $c^{\text{iso}}_{3qr3} = \begin{pmatrix}x_2 & 0 & 0\\ 0 & x_2 & 0\\ 0 & 0 & x_1\end{pmatrix}$ and x_1 and x_2 are any arbitrary positive real numbers.

As expected, LN does not have a cut with an entirely isotropic plane $x'Oy'$ after a simple rotation θ. Instead, the point of this effort is to explore how to *minimize* the anisotropy of the $x'Oy'$ plane. To this end, we seek the minimum of the Euclidean norm of the difference between the anisotropic stiffness tensor in the plane and its isotropic counterpart [37, 38], written as $\min_\theta \mathcal{L}_2 \equiv ||c^{E\prime}_{3qr3} - c^{\text{iso}}_{3qr3}||_2$ by varying

x_1 and x_2 for each specific given angle θ, which describes the specific differences between the in-plane stiffness for $\theta + 90°$ degree Y-cut LN and an analogous isotropic material. In the analysis, the dielectric components are simply assumed to be $\varepsilon_{11} = \varepsilon_{22} = \varepsilon_{33} = 1$ for the isotropic material and are in any case irrelevant to the computations needed in this study. A custom MATLAB (MathWorks, Natick, MA, USA) code was used to calculate and plot the norm $\mathcal{L}_2$ versus $(\theta + 90°)$ as shown in Fig. 1(e) with increments in θ of $0.1°$. For our calculations, LN is presumed to have the following values for the stiffness: $c_{11}^E, c_{12}^E, c_{13}^E, c_{14}^E, c_{33}^E, c_{44}^E, c_{66}^E = 2.030, 0.53, 0.75, 0.09, 2.45, 0.60, 0.75 \times 10^{11}$ N/m^2 [39].

Notably, when $\theta \to 0$ or $180°$—known as *Z-cut LN*—a popular view is that $\min_\theta\{\mathcal{L}_2\}$ should go to zero and the cut is "isotropic in the plane" $x'Oy'$. This is true for the stiffness tensor, as made clear from Fig. 1(d). However, as shown in Fig. 5 in Appendix B, Z-cut LN in fact remains anisotropic in the plane. Instead of using the stiffness tensor, the evidence is provided there by computing the norm of the piezoelectric stress tensor $\mathbf{e}$ for LN versus the zero tensor value for an isotropic material, all upon the plane $x'Oy'$. If the material were truly isotropic in the plane, this value would also go to zero, because the piezoelectricity would be absent in the plane. While the norm of the piezoelectric stress tensor does not go to zero as $\theta \to 0$ or $180°$, it does go to a minimum value. This suggests both the piezoelectric coupling and this particular cut's ability to generate SAW will be poor. In fact, Z-cut LN is known to be poor for surface wave generation and propagation [40]. Despite its in-plane stiffness isotropy, the Z-cut is therefore deemed to be unsuitable and is excluded from further consideration.

Fig. 1(e) indicates two other possibilities for minimization of the anisotropy of LN on the $x'Oy'$ plane: a Y-rotated cut angle of $118°$ $(= (\theta = 28°)+90°)$ and a cut angle of $152°$. The $152°$ Y-rotated cut, in particular, is around the ubiquitous $128°$ YX cut [8] used for SAW, and so Y-rotated cuts around $152°$ may be interesting from the perspective of electromechanical coupling. The $28°$ cut as the other minimum is also a possible choice for SAW generation and propagation while minimizing the effect of anisotropy.

III. Calculation of coupling coefficient for electromechanical properties

There is a universal relationship between the coupling coefficient, K^2, and the open and short-circuited SAW velocities v_o and v_m, respectively [41]:

$$K^2 = \frac{2(v_o - v_m)}{v_o} \tag{7}$$

One approach to determine the effectiveness of any particular Y-rotated cut defined by θ in comparison to the 128YX cut of LN is to determine the surface wave velocities v_o and v_m and then use eqn. (7) to compare the coupling coefficients between $\theta + 90°$ Y-cut LN and $128°$ Y-cut LN.

A. Determining the velocity of open and short-circuited SAW

The set of linear equations describing acoustic wave propagation in an arbitrary, anisotropic piezoelectric medium is, in standard component notation, as follows [12]:

$$\begin{aligned} \frac{\partial T_{ij}}{\partial x_i} &= \rho \frac{\partial^2 u_j}{\partial t^2}, \\ S_{kl} &= \frac{1}{2}\left(\frac{\partial u_k}{\partial x_l} + \frac{\partial u_l}{\partial x_k}\right), \\ \frac{\partial D_i}{\partial x_i} &= 0, \\ E_i &= -\frac{\partial \varphi}{\partial x_i}, \\ T_{ij} &= c'_{ijkl} S_{kl} - e'_{nij} E_n, \\ D_m &= e'_{mkl} S_{kl} + \varepsilon'_{mn} E_n, \end{aligned} \tag{8}$$

where T_{ij} is the stress tensor component, ρ is the mass density, u_j is the mechanical displacement, S_{ij} is the strain tensor component, D_i is the electric displacement, E_i is the electric field, x_i is a spatial coordinate, and φ is the electric potential. The primed quantities refer to a rotated coordinate system in which the stiffness tensor (c'_{ijkl}), the piezoelectric stress tensor (e'_{ijk}), and the permittivity tensor (ε'_{ij}) are given in terms of A_{ij} and the unrotated quantities as follows:

$$\begin{aligned} c'_{ijkl} &= A_{ir} A_{js} A_{kt} A_{ln} c_{rstn}, \\ e'_{ijk} &= A_{ir} A_{js} A_{kt} e_{rst}, \\ \varepsilon'_{ij} &= A_{ir} A_{js} \varepsilon_{rs}. \end{aligned} \tag{9}$$

By simplifying eqns. (8) through substitution of the strain-displacement and electric field strength-electric potential equations into the stress-strain-electric field strength and electric field displacement-strain-field strength equations, then substitution of the result into the momentum equation while ensuring $\partial D_i / \partial x_i = 0$ is enforced, eqns. (8) may be reduced to the following equations:

$$\begin{aligned} c'_{ijkl} u_{k,li} + e'_{kij} \varphi_{,ki} &= \rho \ddot{u}_j, \\ e'_{ikl} u_{k,li} - \varepsilon'_{ik} \varphi_{,ki} &= 0. \end{aligned} \tag{10}$$

The dot notation refers to differentiation with respect to time, while an index preceded by a comma denotes differentiation with respect to a space coordinate. The coordinates are set such that the LN material substrate surface is at $z' = 0$, or plane $x'Oy'$ in Fig. 1(a). The material is located only along $z' < 0$, and so eqns. (8–10) are only valid for $z' < 0$. The region $0 \leqslant z' \leqslant h$ is set to be a thin, perfect electric conductor where Laplace's equation describes the electric potential φ,

$$\nabla^2 \varphi = 0, \tag{11}$$

where $h = 0$ and $h \to \infty$ refer to electrically shorted and open surfaces, respectively.

Equations (10) and (11) together with appropriate boundary conditions form a complete set of governing equations for acoustic wave propagation upon or within an arbitrary, anisotropic piezoelectric medium. Taupin *et al.* [42] recently used a semi-analytical finite element method to study guided wave propagation in viscoelastic multilayered anisotropic plates by computing displacement, dispersion,

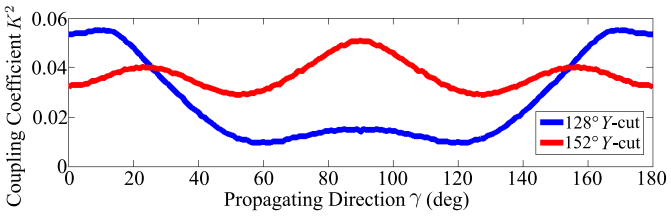

Fig. 2: The calculated electromechanical coupling coefficient, K^2, of Y-cut LN with respect to the propagation direction of the SAW along the $x'Oy'$ plane for 152° Y-cut LN in comparison to 128YX LN. The coupling coefficient is superior in 152° Y-cut LN for propagation angles roughly between 30° and 150° and inferior outside this range.

slowness curves, and energy propagation. Although it cannot be used directly to study surface wave propagation upon a non-viscous piezoelectric material plane as in this case, it is still a useful wave propagation calculation method. Here, we pursued a method detailed in the Appendix and closely related to the classic method defined by Tiersten [12] and Farnell's partial waves method [16] for free and layered infinite half-space problems to determine the SAW propagation velocities in a given direction along a plane.

B. Numerical Calculations and Results of Surface Wave Velocities and Coupling Coefficients

Referring to Appendix C, a transcendental matrix equation may be obtained that, upon solution, produces the SAW velocities for waves upon the $x'Oy'$ plane. Briefly, this equation is obtained from assumption of the form of the propagating SAW, substitution of this form into eqns. (10) and (11) to produce a matrix equation (eqn. (26)). Finding the eigenvalues of that equation produces the SAW velocities, though because the resulting transcendental equation can not be analytically solved, a numerical method is utilized to determine the open and short-circuit SAW velocities.

We first define a particular SAW propagation direction on the $x'Oy'$ surface of the LN, the surface of the LN wafer after performing the $\theta + 90°$ rotation. The direction the SAW propagates on this surface is defined by the angle γ from the material's X axis. Knowing that the velocity of this SAW, v_S, will be in the range of 3000 m/s to 5000 m/s [17, 14], we then determine $\alpha^{(l)}$ from eqn. (22), and obtain the determinant from eqn. (26). Since $h = 0$ and $h = \infty$ correspond to short-circuited and open-circuited surfaces, respectively, finding the minimum of this determinant for each of these two conditions produces the velocities v_m and v_o of the propagating SAW. In order to accurately identify the minima of the determinant, and therefore the velocities v_m and v_o of the propagating SAW, increments of only 1 m/s in the SAW open and short-circuit phase velocities were used for discrete values of γ subtended by $\Delta\gamma = 1°$.

Substituting the calculated velocities v_m and v_o into eqn. (7) produces the associated coupling coefficient K^2 for each value of γ, as shown in Fig. 2. The coupling coefficient for SAW propagating upon the 152° Y-rotated cut is notably larger than upon the 128° Y-rotated cut over a majority of the propagation directions, between $\gamma \approx 30°$ and $\gamma \approx 150°$. Outside this range and, as expected, near the X-propagating direction ($\gamma = 0°$) the traditional 128YX cut of LN is superior.

The 152° Y-cut LN is quantifiably more isotropic in the $x'Oy'$ plane. For example, the standard deviation of the electromechanical coupling coefficient, K^2, over the range $\gamma = 0°$ to 180° using 152° Y-cut LN is 66.5% lower than when using 128° Y-cut LN, indicating an electromechanical coupling coefficient that is more uniform in 152° Y-cut LN. Furthermore, and somewhat surprisingly, the average electromechanical coupling coefficient, K^2, over $\gamma = 0°$ to 180° in 152° Y-rotated cut LN is 37.0% *greater* than 128° Y-cut LN, indicating a greater overall ability to produce SAW. Therefore, for omnidirectional surface wave actuation on LN, a 152° Y-rotated cut LN is significantly both less anisotropic and more electromechanically efficient than the 128° Y-cut, and is superior to other Y-rotated choices. The reader should remember that for *unidirectional* SAW, the 128YX cut remains superior.

IV. Choosing a Cut via the Ratio of the Electromechanical Coupling Coefficient using the Euclidean Norm

The Euclidean norm may been used on the in-plane portion of the stiffness tensor to quantifiably compare anisotropic LN and an arbitrary isotropic material to produce candidate cuts that are more isotropic in the substrate surface plane upon which the SAW propagates. Two cuts were shown to offer greater isotropy than the 128YX cut and therefore may prove to be more useful in acoustofluidic applications. The well-known *Z*-cut of LN that has already been excluded is a good example of why the electromechanical coupling coefficient is as important to consider as the anisotropy: the *Z*-cut is ideally isotropic in the plane but offers very weak electromechanical coupling, making it an unsuitable choice. A somewhat tedious computational method has been provided to determine the electromechanical coupling coefficient for SAW propagating in a given direction defined by γ upon the surface of a $(\theta+90°)$-rotated cut of LN.

A combination of these two aspects are needed to identify a cut of LN that would best serve both purposes—simultaneously improve its in-plane isotropy and electromechanical coupling to generate SAW—that are, to some extent, at odds with each other. In what follows, a remarkably simple method is proposed to identify an optimum θ angle of Y-rotated cut LN which both minimizes the in-plane anisotropy and maximizes the overall planar electromechanical effect among all propagating directions.

We define $\Phi \equiv K_a^2/\mathcal{L}_2$ as a *figure of merit* and the ratio of the averaged coupling coefficient, K_a^2, to the $\mathcal{L}_2$ norm as a single parameter that includes the effects of both the planar anisotropy and electromechanical coupling. The averaged coupling coefficient is defined as

$$K_a^2 \equiv \sum_{\gamma=0°,1°,\cdots}^{180°} K^2/(\frac{180°}{\Delta\gamma}+1) \qquad (12)$$

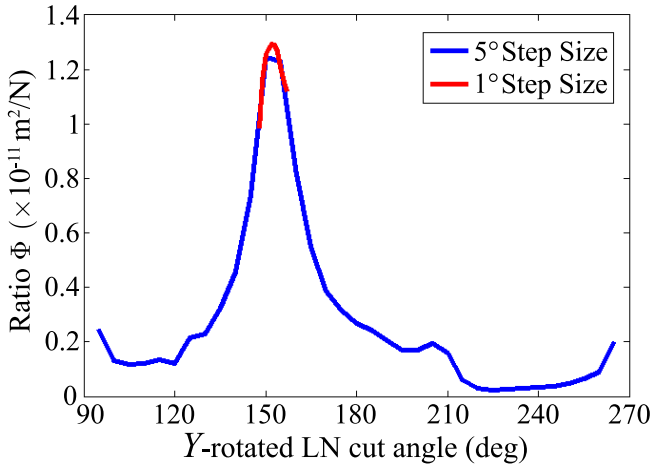

Fig. 3: The ratio, Φ, of the in-plane averaged coupling coefficient over all possible SAW propagation directions, $\gamma \in \{0°, 180°\}$ to the Euclidean norm of the in-plane stiffness tensor between the Y-cut LN and an isotropic material, given by $\Phi \equiv K_a^2/\mathcal{L}_2$, is shown with respect to $\theta + 90°$, the Y-rotated cut angle of LN. The maximum value for Φ is at $\theta + 90° = 152°$, indicating maximal improvements in the isotropy or electromechanical coupling. Another candidate, at $\theta + 90° = 28° + 180°$, exhibits a local minimum in Fig. 1, but shows relatively poor electromechanical coupling, and consequently is omitted from further consideration.

for each specific cut angle, θ, of Y-rotated LN, where $\Delta\gamma = 1°$ is the angular step size used in determining the coupling coefficient values as a function of the SAW propagation direction, and later in calculating a discrete average of the coupling coefficient for all propagation directions upon the Y-rotated cut, $\theta + 90°$ (i.e., the $x'Oy'$ plane). The larger the value of Φ, the overall in-plane electromechanical effect will be greater or the material's anisotropy will be reduced—or both. Maximizing Φ with respect to the Y-rotated cut, $\theta + 90°$, will then correspond to the optimal choice that collectively minimizes anisotropy and maximizes the electromechanical coupling for use in multi-directional SAW propagation.

Considering the computational cost of these calculations and the fact that the relevant material properties are at least smooth to second order (class $\mathcal{C}^2$ as required by eqns. (8)), a low-resolution-calculation of the cumulative coupling coefficient for $\theta = 0°$ to $180°$ in $5°$ steps and 5 m/s increments in the SAW open and short-circuit phase velocities was first used. According to Yamanouchi *et al.* [43], the velocity of traveling SAW is slower than leaky SAW on Y-cut LN. Thus, we identified the slower traveling SAW velocity by finding the local minimum of the determinant from eqn. (26). Figure 3 shows the result, where the highest value of Φ occurs between $\theta + 90° = 145°$ and $155°$. To more accurately determine the specific optimum, a higher-resolution calculation of $\Phi = K_a^2/\mathcal{L}_2$ was conducted from $\theta + 90° = 145°$ to $155°$ in $1°$ steps and 1 m/s increments for the SAW open and short-circuit phase velocities. As shown in Fig. 3, the $\theta + 90° = 152°$ Y-rotated cut produces the maximum $K_a^2/\mathcal{L}_2$ of any value of θ for LN, representing the optimum choice to minimize planar anisotropy and maximize planar electromechanical coupling in multi-directional SAW propagation applications. More accurate calculations to further refine $\theta + 90°$ between $151.5°$ and $152.5°$ could be conducted, though most suppliers of LN are unable to economically produce small batches of LN with a custom orientation at an accuracy better than $0.5°$.

V. Experimental Methods and Results

To compare with our computational results, we designed and fabricated a series of SAW interdigital transducer devices on double-side polished $152°$ Y-rotated cut LN (Jiaozuo Commercial FineWin Co., Ltd, Jiaozuo, Henan, China) for surface acoustic wave generation and propagation.

A. Device Design and Fabrication

As depicted in Fig. 4(a), twenty-four finger pairs were used in each of fifteen interdigital transducers (IDT) arranged in a circular pattern about a central point with $24°$ of angular separation between them. A wavelength of $\lambda = 100$ μm was selected for an operating frequency of ~ 40 MHz (from $f = v/\lambda$) to define each IDT, comprised of twenty simple finger pairs with finger and gap widths of $\lambda/4$ and an aperture of 2 mm. For lithium niobate wafers of 500 μm thickness, 40 MHz is approximately the minimum frequency that may be used to generate useful Rayleigh SAW. Lower frequencies typically reported in much of the acoustofluidics literature are actually generating Lamb waves instead [2]. Standard UV photolithography (using AZ 1512 photoresist and AZ 300MIF developer, MicroChem, Westborough, MA) was used alongside sputter deposition and lift-off processes to fabricate the 10 nm Cr / 1 μm Al IDT upon the 500 μm thick LN substrate [2]. Absorbers (Dragon Skin™, Smooth-On, Inc., Macungie, PA) were used at the center and periphery of the device to prevent edge reflections and spurious bulk waves. SAW was generated by applying a sinusoidal electric field to the IDT at resonance using a signal generator (WF1967 multifunction generator, NF Corporation, Yokohama, Japan) and amplifier (ZHL–1–2W–S+, Mini-Circuits, Brooklyn, NY, USA). The actual voltage, current, and power across the device were measured using an oscilloscope (InfiniiVision 2000 X-Series, Keysight Technologies, Santa Rosa, CA). The spatiotemporal variations in the wave displacement and velocity amplitudes along the underlying substrate were measured using a laser Doppler vibrometer (LDV, UHF–120, Polytec, Waldbronn, Germany).

B. Experimental Data and Analysis

Instantaneous displacement and phase measurements were made using the LDV along the propagation directions determined by the placement of the IDTs in Fig. 4(a). For example, Fig. 4(b) illustrates the SAW amplitude and phase propagating along the $\gamma = 108°$ direction, with 807 mW at 33.956 MHz AC input applied on the device, demonstrating the generation of traveling surface acoustic waves. With a standing wave ratio (SWR) of 1.47, the results indicate a good

traveling SAW propagating across the 152° Y-rotated cut LN $x'Oy'$ surface. The SWR is the ratio of the maximum and minimum amplitude of the wave, measured over at least one wavelength, indicating a pure traveling wave when SWR $= 1$ and a pure standing wave when SWR $\to \infty$. To compare the experimental and computational results, the relative energy $E \propto A^2$ was used and scaled to fit the computational results, correlating the amplitude of the SAW on LN surface with the electromechanical coupling energy [8]. The amplitudes, A, in each propagation direction are averaged among the LDV scanning region to reduce the effects of aliasing from the pointwise measurement of the scanning LDV. As shown in Fig. 4(c), the experimental and computational results produce a high correlation coefficient of 0.93, a good fit, verifying the results of the calculations and the underlying method to arrive at a useful cut.

VI. Conclusions

A technique to consistently optimize the Y-axis rotation angle for a competing set of design characteristics has been provided. It has been used to minimize the in-plane anisotropy and maximize the electromechanical coupling to enable multi-directional generation and propagation of SAW upon LN. Producing three candidates—Z-cut, 28° Y-rotated cut, and 152° Y-rotated cut LN—the method ultimately indicates the 152° Y-rotated cut as the superior choice. Compared to the 128YX cut of LN used for virtually all of today's acoustofluidic devices, this cut provides a 66.5% improvement in the in-plane isotropy for SAW propagating in any direction upon the LN substrate, and a 37.0% improvement in the average electromechanical coupling when attempting to propagate SAW in any direction. While the 128YX cut remains the best choice for unidirectional SAW along the X axis, the 152° Y-rotated cut offers significant advantages in those applications for which SAW propagation in other directions is desirable.

The technique combines classic analysis approaches with an $\mathcal{L}_2$-norm comparison of the stiffness and piezoelectric stress tensor to an isotropic analogue while varying the Y-rotated cut angle $\theta + 90°$. To determine the effect of these rotations upon the equally important electromechanical coupling of SAW propagating along any direction on the plane of the Y-rotated substrate for each value of θ, a physical model with closed-form governing equations for SAW propagation on the surface of a piezoelectric material was used to obtain open and short-circuit SAW phase velocities. These velocities were then used to compute the averaged coupling coefficient over all possible SAW propagation directions upon the LN substrate, defined by γ with respect to the X axis. Next, a figure of merit composed of a ratio of the averaged coupling coefficient to the Euclidean norm of the planar anisotropy, $\Phi = K_a^2/\mathcal{L}_2$, was defined and used to determine the value of θ that minimizes the in-plane anisotropy and maximizes the electromechanical coupling. This procedure produced the 152° Y-rotated cut of LN as the clearly optimal choice.

Finally, an experimental device was designed, fabricated, and tested using the 152° Y-cut LN substrate, serving not only to verify the analysis and calculations, but also demonstrating the ability to effectively form SAW in directions other than along the X axis as a practical demonstration of the continued utility of lithium niobate for the demanding requirements of acoustofluidics. This technique can be adapted to serve other materials, other orientations, and other design goals as required, providing a new perspective in materials selection in acoustics and ultrasound as built upon the comprehensive analysis framework provided in the past.

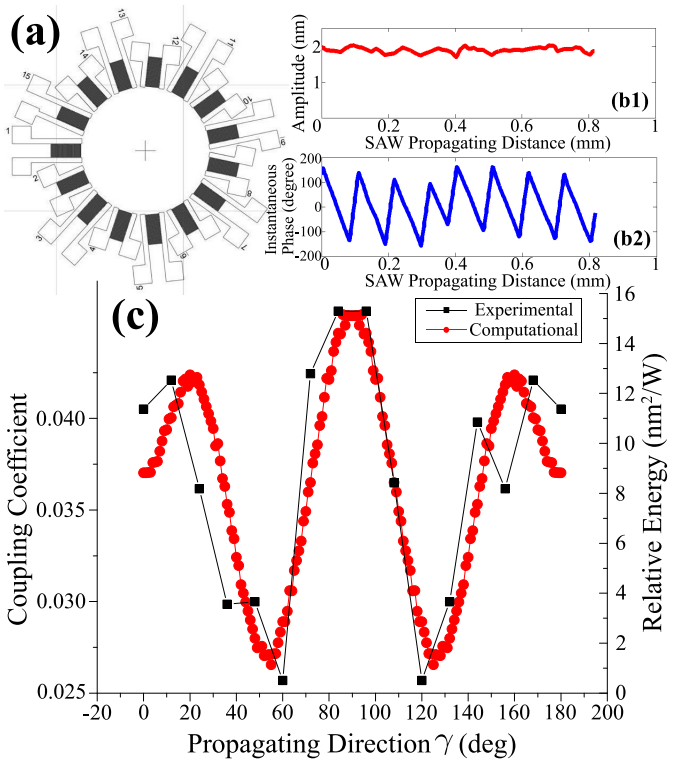

Fig. 4: Our (a) experimental IDT configuration for testing the ability to generate and propagate SAW across the surface of the rotated LN cut. As an example, the (b) spatial distribution of the instantaneous displacement and phase of the LN substrate transverse to plane $x'Oy'$ along $\gamma = 108°$ shows a good quality traveling SAW with SWR$= 1.47$. A measure of the energy of the SAW with respect to its propagation direction is (c) provided for the fifteen directions defined by the IDTs in our (a) experiment upon 152° Y-rotated cut LN. This closely corresponds to the numerically determined coupling coefficient provided in the same figure: since the data is not normally distributed, a Wilcoxon signed rank pairwise test for unequal data sets produces a p-value of 4.98×10^{-10}, well within the typical $p < 0.01$, indicating the veracity of the analysis in representing the experimental outcome. The lines provided are solely shown as a guide to the eye.

Appendix A
Customary Definition and Representations of the Stiffness, Piezoelectric, and Dielectric Tensors

The stiffness tensor c_{ijkl} is a fourth-order tensor where the number of coefficients is $3^4 = 81$. But due to the symmetry of the tensor, we have $c_{ijkl} = c_{jilk} = c_{ijlk} = c_{jikl}$ and

the number of independent coefficients is reduced to 36. It is customary to reduce the fourth-order tensors to a second-order (Voigt) representation $c_{ijkl} = c_{\alpha\beta}$ where $i, j, k, l \in 1, 2, 3$ and $\alpha, \beta \in 1, 2, 3, 4, 5, 6$: $(11) \leftrightarrow 1, (22) \leftrightarrow 2, (33) \leftrightarrow 3, (23) = (32) \leftrightarrow 4, (31) = (13) \leftrightarrow 5, (12) = (21) \leftrightarrow 6$. In the same way, the third-order piezoelectric tensor can be represented as a 3×6 matrix. Thus, the stiffness, piezoelectric, and dielectric tensors' matrix representations are combined together into one (*see* Fig. 1(a–c)):

$$\begin{bmatrix} \mathbf{c}^E & \underset{\sim}{\mathbf{e}} \\ \mathbf{e} & \underset{\sim}{\boldsymbol{\varepsilon}}^S \end{bmatrix}, \tag{13}$$

where c^E is a reduced 6×6 stiffness matrix; e is reduced 3×6 piezoelectric stress matrix; $\underset{\sim}{e}$ is the transpose of the reduced 3×6 piezoelectric stress matrix; $\underset{\sim}{\varepsilon}^S$ is the transpose of the 3×3 dielectric matrix, such that each $\cdot$ represents a zero value, the $\bullet$ and $\circ$ represent non-zero values, the connecting lines between non-zero values indicate equality, and a line connecting a $\bullet$ and $\circ$ indicate these values have opposing signs. The $\times$ symbol represents $(c_{11} - c_{12})/2$. Figure 1(b) shows the tensors' matrix representations of the 3m crystal material according to a coordinate system formed from the crystal's principal axes.

Appendix B
Analysis of Piezoelectric Stress Tensor of LN to Quantify the In-Plane Isotropy

Similar to the analysis of the stiffness tensor in Section II, here we investigate the in-plane anisotropy present in a given cut of LN via the piezoelectric stress tensor. Closely following the method described in Section II, we have

$$e'_{pqr} = e_{ijk} A_{ip} A_{jq} A_{kr}, \tag{14}$$

for the piezoelectric stress tensor where

$$[A] = \begin{pmatrix} 1 & 0 & 0 \\ 0 & \cos\theta & -\sin\theta \\ 0 & \sin\theta & \cos\theta \end{pmatrix}.$$

To investigate the *planar* anisotropy of the surface plane $x'Oy'$ of $(\theta+90^\circ)$-rotated LN, a double inner product between the unit vector $\mathbf{e}'_3$ normal to the substrate surface and the piezoelectric tensor in the rotated coordinate system shown in eqn. (14) may be taken;

$$\mathbf{e}'_3 \cdot (e'_{pqr} \mathbf{e}'_p \mathbf{e}'_q \mathbf{e}'_r) \cdot \mathbf{e}'_3 = e'_{3q3} \mathbf{e}'_q. \tag{15}$$

As isotropic materials do not have piezoelectricity, all components of the piezoelectric stress tensor for an isotropic material must be zero:

$$e^{\text{iso}}_{ijk} \equiv 0 \text{ for all } i, j, k \in \{1, 2, 3\}. \tag{16}$$

Taking into account the $3m$ crystal class of LN, the $\mathcal{L}_2$ norm of the in-plane components of the piezoelectric stress tensor of LN in comparison to an isotropic material may be written as

$$e_{\text{norm}} = \sqrt{e'^{\,2}_{313} + e'^{\,2}_{323} + e'^{\,2}_{333}}; \tag{17}$$

e_{norm} represents not only the electromechanical coupling of LN, but also the magnitude of the in-plane anisotropy of the piezoelectric stress tensor. This quantity strongly depends upon the LN Y-rotated cut angle $\theta + 90^\circ$.

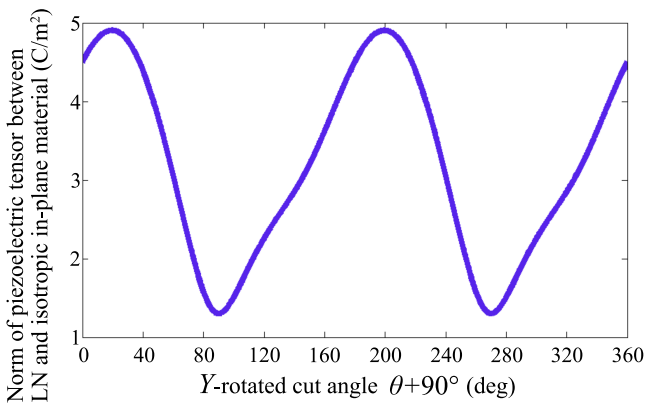

Fig. 5: A plot of the norm of the change in the piezoelectric tensor between the as-rotated cut of LN and an isotropic-in-the-plane material—with zero piezoelectric response. The Y-rotated cut angle is $\theta + 90^\circ$. The positive, non-zero value of e_{norm} for all values of $\theta + 90^\circ$ indicates LN always has piezoelectric properties in the plane, and therefore must likewise always be anisotropic in the plane.

A custom code (MATLAB, MathWorks, Natick, MA, USA) was used to calculate and plot e_{norm} versus $\theta + 90^\circ$ as shown in Fig. 5 with increments in θ of 0.1°. The positive value of e_{norm} indicates the extent of the substrate's anisotropy in the plane: a larger value indicates a greater anisotropy. Seeking the minimum value of the anisotropy is straightforward from this plot: the minimum of e_{norm} is $\theta + 90^\circ \rightarrow 90^\circ$ or 270°, in other words *Z*-cut LN. However, the result also indicates a small coupling coefficient for these values of $\theta + 90^\circ$, and consequently a relatively poor ability to generate SAW. Thus one must also take into account the electromechanical coupling, and not just the anisotropy.

Appendix C
Method to Determine the Open and Short-Circuit SAW Phase Velocity

To investigate the phase velocity of SAW upon the Y-rotated LN substrate surface, we first perform a rotational transformation about the x axis by an angle θ to produce the substrate surface plane $x'Oy'$ upon which the SAW will be made to propagate. To make the SAW propagate in a direction defined by γ from the positive x axis, we apply a second rotational transformation about the z' axis by an angle γ. Similar in appearance to eqns. (9), the stiffness tensor (c''_{wxyz}), the piezoelectric stress tensor (e''_{wxy}), and the permittivity tensor (ε''_{wx}) are the corresponding material property tensors after these rotational transformations:

$$\begin{aligned} c''_{wxyz} &= B_{wi} B_{xj} B_{yk} B_{zl} c'_{ijkl}, \\ e''_{wxy} &= B_{wi} B_{xj} B_{yk} e'_{ijk}, \\ \varepsilon''_{wx} &= B_{wi} B_{xj} \varepsilon'_{ij}, \end{aligned} \tag{18}$$

where the rotational transformation matrix may be written as

$$B = \begin{pmatrix} \cos\gamma & -\sin\gamma & 0 \\ \sin\gamma & \cos\gamma & 0 \\ 0 & 0 & 1 \end{pmatrix}. \tag{19}$$

We use the Voigt contracted notation for the tensors $c_{\alpha\beta}$, $e_{w\alpha}$, ε_{wx} instead of c''_{wxyz}, e''_{wxy}, ε''_{wx} by exploiting the material symmetry, noting $w, x, y, z \in 1, 2, 3$ and $\alpha, \beta \in 1, 2, 3, 4, 5, 6$: $(11) \leftrightarrow 1, (22) \leftrightarrow 2, (33) \leftrightarrow 3, (23) = (32) \leftrightarrow 4, (31) = (13) \leftrightarrow 5, (12) = (21) \leftrightarrow 6$. After rotational transformation of θ about the x axis to produce the coordinate system $Ox'y'z'$, we use a second rotational transformation of γ about the z' axis to produce the coordinate system $Ox''y''z'$ and seek solutions for the open and short-circuit SAW phase velocity along the x'' axis, noting that z'' and z' are coincident.

In this section of the Appendix, we denote x'' as x_1, y'' as x_2, and z'' as $-x_3$ to produce a general solution for the open and short-circuited phase velocities of SAW in the $Ox_1x_2x_3$ coordinate system.

Solutions of eqns. (10) and (11) are assumed to be of the standard traveling-wave form in which v_S is the wave velocity and α describes the exponential decay of the SAW into the crystal such that

$$\begin{aligned} u_i &= \beta_i e^{-\alpha\omega x_3/v_S} e^{j\omega(t-x_1/v_S)} \\ \varphi &= \beta_4 e^{-\alpha\omega x_3/v_S} e^{j\omega(t-x_1/v_S)} \end{aligned} \quad i \in \{1, 2, 3\}. \tag{20}$$

As indicated above, the surface waves under consideration are assumed to be travelling in the x_1 direction. The displacements and potentials are considered to be independent of the x_2 coordinate.

Substituting eqns. (20) into eqns. (10) and (11) produces a linear homogeneous system of four equations with four unknowns, β_1, β_2, β_3, and β_4:

$$\begin{pmatrix} c_{55}\alpha^2 + 2c_{15}j\alpha - c_{11} + \rho v_S^2, & c_{45}\alpha^2 + (c_{14}+c_{56})j\alpha - c_{16}, & c_{35}\alpha^2 + (c_{13}+c_{55})j\alpha - c_{15}, & e_{35}\alpha^2 + (e_{15}+e_{31})j\alpha - e_{11} \\ c_{45}\alpha^2 + (c_{14}+c_{56})j\alpha - c_{16}, & c_{44}\alpha^2 + 2c_{46}j\alpha - c_{66} + \rho v_S^2, & c_{34}\alpha^2 + (c_{36}+c_{45})j\alpha - c_{56}, & e_{34}\alpha^2 + (e_{14}+e_{36})j\alpha - e_{16} \\ c_{35}\alpha^2 + (c_{13}+c_{55})j\alpha - c_{15}, & c_{34}\alpha^2 + (c_{36}+c_{45})j\alpha - c_{56}, & c_{33}\alpha^2 + 2c_{35}j\alpha - c_{55} + \rho v_S^2, & e_{33}\alpha^2 + (e_{13}+e_{35})j\alpha - e_{15} \\ e_{35}\alpha^2 + (e_{15}+e_{31})j\alpha - e_{11}, & e_{34}\alpha^2 + (e_{14}+e_{36})j\alpha - e_{16}, & e_{33}\alpha^2 + (e_{13}+e_{35})j\alpha - e_{15}, & -\varepsilon_{33}\alpha^2 - 2\varepsilon_{13}j\alpha + \varepsilon_{11} \end{pmatrix} \begin{pmatrix} \beta_1 \\ \beta_2 \\ \beta_3 \\ \beta_4 \end{pmatrix} = \begin{pmatrix} 0 \\ 0 \\ 0 \\ 0 \end{pmatrix}. \tag{21}$$

The determinant of the 4×4 matrix at left must be zero for a non-trivial solution to exist, producing

$$\begin{aligned} A_8\alpha^8 + jA_7\alpha^7 + A_6\alpha^6 + jA_5\alpha^5 + A_4\alpha^4 \\ + jA_3\alpha^3 + A_2\alpha^2 + jA_1\alpha + A_0 = 0, \end{aligned} \tag{22}$$

where the coefficients A_n with $n = 0, 1, ..., 8$ are real and a particular value of v_S has been assumed. Since the electromechanical fields must be finite, they must go to zero as $x_3 \to \infty$, and so only the roots with non-negative real parts are allowed. If the unknown in eqn. (22) is considered to be $j\alpha$ instead of α, then the polynomial in $j\alpha$ has purely real coefficients. Thus, either the roots $j\alpha$ are real or occur in conjugate pairs. Therefore, the roots α are either purely imaginary or occur in pairs with positive and negative real parts. In general, four roots with positive real parts occur for piezoelectric crystals. Upon obtaining the admissable values of α from eqn. (22), the corresponding values of β_i can be found for each α from eqn. (21).

In addition to the equations for $x_3 > 0$, the differential eqn. (11) for $-h \leqslant x_3 \leqslant 0$ must be satisfied together with appropriate boundary conditions at $x_3 = 0$ and $x_3 = -h$. Assuming that the crystal surface is stress free ($T_{3j} = 0$ at $x_3 = 0$), the mechanical boundary conditions at each point of the surface of the crystal are

$$T_{3j}|_{x_3=0} = c_{3jkl}u_{k,l} + e_{k3j}\varphi_{,k}|_{x_3=0} = 0; \quad j \in \{1, 2, 3\}. \tag{23}$$

The boundary conditions for the electric potential are continuity of φ at $x_3 = 0$ and, without loss of generality, $\varphi(-h) = 0$. Also, the normal component of the electrical displacement must be continuous across the surface of the crystal. The combined electromechanical fields (mechanical displacement and electric potential) may be expressed as a linear combination of the fields associated with the admissible values of α for $x_3 > 0$, following the method shown by Farnell and other many years ago as the *concept of partial waves*[44, 16], that is,

$$\begin{aligned} u_i &= \sum_{l=1}^{4} B^{(l)}\beta_i^{(l)} e^{-\alpha^{(l)}\omega x_3/v_S} e^{j\omega(t-x_1/v_S)}, \\ \varphi &= \sum_{l=1}^{4} B^{(l)}\beta_4^{(l)} e^{-\alpha^{(l)}\omega x_3/v_S} e^{j\omega(t-x_1/v_S)}, \end{aligned} \tag{24}$$

with $i \in \{1, 2, 3\}$. In the region $-h \leqslant x_3 \leqslant 0$, the potential is a solution of Laplace's eqn. (11). A solution satisfying the continuity condition at $x_3 = -h$ is

$$\varphi = \sum_{l=1}^{4} B^{(l)}\beta_4^{(l)} \operatorname{csch}(\frac{\omega h}{v_S}) \sinh(\frac{\omega}{v_S}(x_3 + h)) e^{j\omega(t-x_1/v_S)}. \tag{25}$$

Finally, the component of $\mathbf{D}$ normal to the surface $x_3 = 0$, D_3, must be continuous across the surface. Inside the crystal the electrical displacement is given by $D_i = e_{ikl}u_{k,l} - \varepsilon_{ik}\varphi_{,k}$, while in the region $-h \leqslant x_3 \leqslant 0$, $\mathbf{D} = -\varepsilon_0\nabla\varphi$. Substituting the expressions for the waves in eqns. (24) in eqn. (23) and expressing the continuity of D_3 at $x_3 = 0$ in terms of eqns. (24) produces the following set of homogeneous

equations for the so-called *partial field amplitudes* $B^{(l)}$:

$$\begin{aligned}
&\sum_{l=1}^{4}(\beta_1^{(l)}(jc_{15}+\alpha^{(l)}c_{55})+\beta_2^{(l)}(jc_{56}+\alpha^{(l)}c_{45})\\
&+\beta_3^{(l)}(jc_{55}+\alpha^{(l)}c_{35})+\beta_4^{(l)}(je_{15}+\alpha^{(l)}e_{35}))B^{(l)}=0\\
&\sum_{l=1}^{4}(\beta_1^{(l)}(jc_{14}+\alpha^{(l)}c_{45})+\beta_2^{(l)}(jc_{46}+\alpha^{(l)}c_{44})\\
&+\beta_3^{(l)}(jc_{45}+\alpha^{(l)}c_{34})+\beta_4^{(l)}(je_{14}+\alpha^{(l)}e_{34}))B^{(l)}=0\\
&\sum_{l=1}^{4}(\beta_1^{(l)}(jc_{13}+\alpha^{(l)}c_{35})+\beta_2^{(l)}(jc_{36}+\alpha^{(l)}c_{34})\\
&+\beta_3^{(l)}(jc_{35}+\alpha^{(l)}c_{33})+\beta_4^{(l)}(je_{13}+\alpha^{(l)}e_{33}))B^{(l)}=0\\
&\sum_{l=1}^{4}(\beta_1^{(l)}(je_{31}+\alpha^{(l)}e_{35})+\beta_2^{(l)}(je_{36}+\alpha^{(l)}e_{34})\\
&+\beta_3^{(l)}(je_{35}+\alpha^{(l)}e_{33})-\\
&\beta_4^{(l)}(j\varepsilon_{13}+\alpha^{(l)}\varepsilon_{33}+\varepsilon_0\coth(\frac{\omega h}{v_S})))B^{(l)}=0.
\end{aligned} \tag{26}$$

The transcendental equation obtained by setting the determinant of the matrix of coefficients of this system equal to zero determines the surface wave velocities for a given set of $\alpha^{(l)}$ [17, 14]. This set of transcendental equations is known to lack any explicit solutions [45]. Thus we use numerical analysis to identify the open and short-circuit SAW phase velocities $v_o = v_S$ and $v_m = v_S$ when $\omega h = \infty$ and $\omega h = 0$ respectively, as detailed in Section III.B.

The open and short-circuit SAW phase velocities v_o and v_m determined from this process for propagation upon the surface of 152° and 128° Y-rotated cut LN are shown in Fig. 6(a,b). The phase velocities are plotted with respect to the angle γ between the SAW propagation direction and the X axis, indicating that the differences in surface wave velocities between 152° and 128° Y-rotated cut LN are minor.

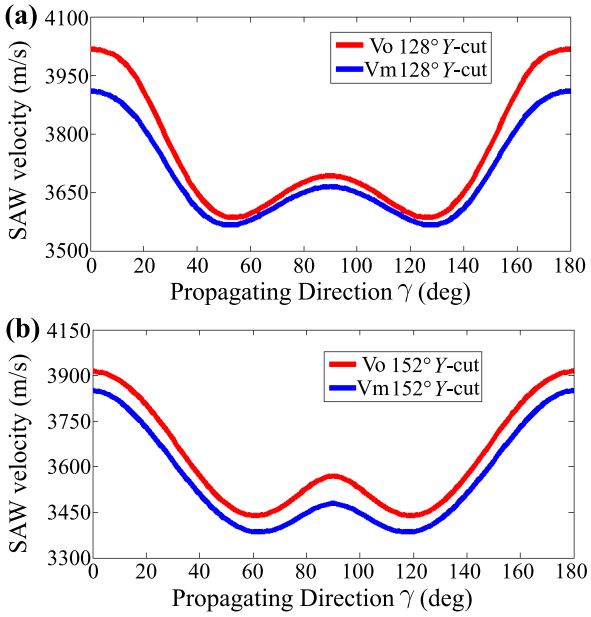

Fig. 6: The open-circuit and short-circuit SAW phase velocity on the surface of (a) 128° Y-cut LN and (b) 152° Y-cut LN plotted with respect to the propagation direction defined by the angle γ measured from the X axis of the LN substrate.

APPENDIX D
LDV SCAN OF INSTANTANEOUS WAVE DISPLACEMENT AND PHASE ALONG A SPECIFIC PROPAGATION DIRECTION

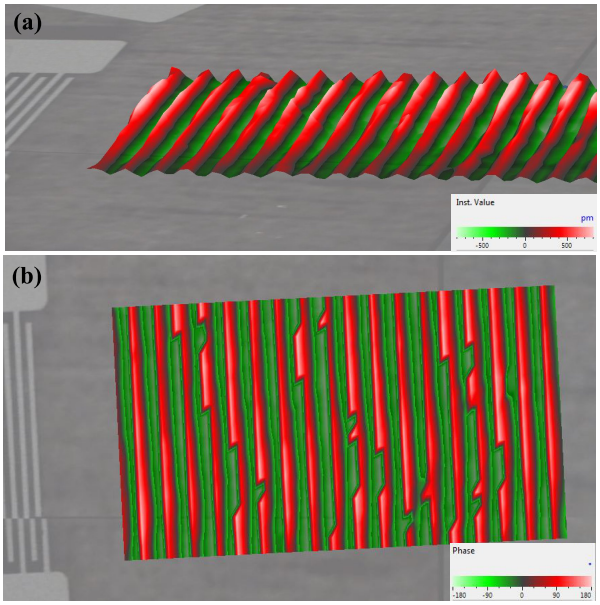

Fig. 7: Laser Doppler vibrometer scans of (a) instantaneous amplitude and (b) phase of SAW generated by the IDTs along the $\gamma = 108°$ direction; the other IDTs produce similar results. Note the finger width and gap between the fingers is $\lambda/4 = 25$ μm in these plots indicating the scale.

ACKNOWLEDGMENTS

The authors are grateful to the University of California and the NANO3 facility at UC San Diego for provision of funds

and facilities in support of this work. This work was performed in part at the San Diego Nanotechnology Infrastructure (SDNI) of UCSD, a member of the National Nanotechnology Coordinated Infrastructure, which is supported by the National Science Foundation (Grant ECCS–1542148). The work presented here was generously supported by a research grant from the W.M. Keck Foundation. The authors are also grateful for the support of this work by the Office of Naval Research (via Grant 12368098), and substantial technical support by Polytec's staff in Irvine, CA and Waldbronn, Germany.

REFERENCES

[1] J. Friend and L. Y. Yeo, "Microscale acoustofluidics: Microfluidics driven via acoustics and ultrasonics," *Reviews of Modern Physics*, vol. 83, no. 2, p. 647, 2011.

[2] W. Connacher, N. Zhang, A. Huang, J. Mei, S. Zhang, T. Gopesh, and J. Friend, "Micro/nano acoustofluidics: materials, phenomena, design, devices, and applications," *Lab on a Chip*, 2018.

[3] X. Ding, P. Li, S.-C. S. Lin, Z. S. Stratton, N. Nama, F. Guo, D. Slotcavage, X. Mao, J. Shi, F. Costanzo *et al.*, "Surface acoustic wave microfluidics," *Lab on a Chip*, vol. 13, no. 18, pp. 3626–3649, 2013.

[4] M. Miansari and J. R. Friend, "Acoustic nanofluidics via room-temperature lithium niobate bonding: A platform for actuation and manipulation of nanoconfined fluids and particles," *Advanced Functional Materials*, vol. 26, no. 43, pp. 7861–7872, 2016.

[5] S.-C. S. Lin, X. Mao, and T. J. Huang, "Surface acoustic wave (SAW) acoustophoresis: now and beyond," *Lab on a Chip*, vol. 12, no. 16, pp. 2766–2770, 2012.

[6] S. Collignon, O. Manor, and J. Friend, "Improving and predicting fluid atomization via hysteresis-free thickness vibration of lithium niobate," *Advanced Functional Materials*, vol. 28, no. 1704359, 2018.

[7] A. Kawamata, H. Hosaka, and T. Morita, "Non-hysteresis and perfect linear piezoelectric performance of a multilayered lithium niobate actuator," *Sensors and Actuators A: Physical*, vol. 135, no. 2, pp. 782–786, 2007.

[8] K. Shibayama, K. Yamanouchi, H. Sato, and T. Meguro, "Optimum cut for rotated Y-cut $LiNbO_3$ crystal used as the substrate of acoustic-surface-wave filters," *Proceedings of the IEEE*, vol. 64, no. 5, pp. 595–597, 1976.

[9] A. Slobodnik and E. Conway, "New high-frequency high-coupling low-beam-steering cut for acoustic surface waves on $LiNbO_3$," *Electronics Letters*, vol. 6, no. 6, pp. 171–173, 1970.

[10] M. Kurosawa, N. Takahashi, and T. Higuchi, "An ultrasonic XY stage using 10 MHz surface acoustic waves," in *Ultrasonics Symposium, 1994. Proceedings., 1994 IEEE*, vol. 1. IEEE, 1994, pp. 535–538.

[11] M. Kurosawa, M. Takahashi, and T. Higuchi, "Ultrasonic linear motor using surface acoustic waves," *IEEE Transactions on Ultrasonics, Ferroelectrics, and Frequency Control*, vol. 43, no. 5, pp. 901–906, 1996.

[12] H. F. Tiersten, "Wave propagation in an infinite piezoelectric plate," *The Journal of the Acoustical Society of America*, vol. 35, no. 2, pp. 234–239, 1963.

[13] J. Lothe and D. Barnett, "Integral formalism for surface waves in piezoelectric crystals. existence considerations," *Journal of Applied Physics*, vol. 47, no. 5, pp. 1799–1807, 1976.

[14] D. Barnett and J. Lothe, "Free surface (Rayleigh) waves in anisotropic elastic half-spaces: the surface impedance method," *Proceedings of the Royal Society of London. A. Mathematical and Physical Sciences*, vol. 402, no. 1822, pp. 135–152, 1985.

[15] M. Destrade, "Rayleigh waves in symmetry planes of crystals: explicit secular equations and some explicit wave speeds," *Mechanics of Materials*, vol. 35, no. 9, pp. 931–939, 2003.

[16] W. G. Farnell, "Types and properties of surface waves," in *Acoustic surface waves*. Springer, 1978, pp. 13–60.

[17] Y. B. Fu and A. Mielke, "A new identity for the surface–impedance matrix and its application to the determination of surface-wave speeds," *Proceedings of the Royal Society of London. Series A: Mathematical, Physical and Engineering Sciences*, vol. 458, no. 2026, pp. 2523–2543, 2002.

[18] A. Darinskii and A. Shuvalov, "Surface acoustic waves on one-dimensional phononic crystals of general anisotropy: Existence considerations," *Physical Review B*, vol. 98, no. 2, p. 024309, 2018.

[19] B. Collet, "Recursive surface impedance matrix methods for ultrasonic wave propagation in piezoelectric multilayers," *Ultrasonics*, vol. 42, no. 1-9, pp. 189–197, 2004.

[20] L. Wang and S. Rokhlin, "Stable reformulation of transfer matrix method for wave propagation in layered anisotropic media," *Ultrasonics*, vol. 39, no. 6, pp. 413–424, 2001.

[21] A. Darinskii, M. Weihnacht, and H. Schmidt, "Resonant reflection of a surface acoustic wave from strip waveguides," *Wave Motion*, vol. 50, no. 8, pp. 1185–1196, 2013.

[22] A. Shuvalov, E. Le Clezio, and G. Feuillard, "The state-vector formalism and the peano-series solution for modelling guided waves in functionally graded anisotropic piezoelectric plates," *International Journal of Engineering Science*, vol. 46, no. 9, pp. 929–947, 2008.

[23] A. N. Darinskii and M. Weihnacht, "Gap acousto-electric waves in structures of arbitrary anisotropy," *IEEE Transactions on Ultrasonics, Ferroelectrics, and Frequency Control*, vol. 53, no. 2, pp. 412–419, 2006.

[24] A. Darinskii and M. Weihnacht, "Interface waves on the sliding contact between identical piezoelectric crystals of general anisotropy," *Wave Motion*, vol. 43, no. 1, pp. 67–77, 2005.

[25] A. Shuvalov, O. Poncelet, and M. Deschamps, "Analysis of the dispersion spectrum of fluid-loaded anisotropic plates: leaky-wave branches," *Journal of Sound and Vibration*, vol. 296, no. 3, pp. 494–517, 2006.

[26] S. Xu and Z. L. Wang, "One-dimensional ZnO nanostructures: solution growth and functional properties," *Nano Research*, vol. 4, no. 11, pp. 1013–1098, 2011.

[27] N. Setter, D. Damjanovic, L. Eng, G. Fox, S. Gevorgian, S. Hong, A. Kingon, H. Kohlstedt, N. Park, G. Stephen-

son *et al.*, "Ferroelectric thin films: Review of materials, properties, and applications," *Journal of Applied Physics*, vol. 100, no. 5, p. 051606, 2006.
[28] Y. Q. Fu, J. Luo, N.-T. Nguyen, A. Walton, A. J. Flewitt, X.-T. Zu, Y. Li, G. McHale, A. Matthews, E. Iborra *et al.*, "Advances in piezoelectric thin films for acoustic biosensors, acoustofluidics and lab-on-chip applications," *Progress in Materials Science*, vol. 89, pp. 31–91, 2017.
[29] G.-Q. Zhang, K.-y. Hashimoto, and M. Yamaguchi, "Liquid streaming by high-frequency ultrasonic waves," *Japanese Journal of Applied Physics*, vol. 35, no. 5S, p. 3248, 1996.
[30] J. W. Kwon, H. Yu, Q. Zou, and E. S. Kim, "Directional droplet ejection by nozzleless acoustic ejectors built on ZnO and PZT," *Journal of Micromechanics and Microengineering*, vol. 16, no. 12, p. 2697, 2006.
[31] C.-Y. Lee, W. Pang, H. Yu, and E. S. Kim, "Subpicoliter droplet generation based on a nozzle-free acoustic transducer," *Applied Physics Letters*, vol. 93, no. 3, p. 034104, 2008.
[32] H. Yu, Q. Zou, J. W. Kwon, D. Huang, and E. S. Kim, "Liquid needle," *Journal of microelectromechanical systems*, vol. 16, no. 2, pp. 445–453, 2007.
[33] S. Tran, P. Marmottant, and P. Thibault, "Fast acoustic tweezers for the two-dimensional manipulation of individual particles in microfluidic channels," *Applied Physics Letters*, vol. 101, no. 11, p. 114103, 2012.
[34] X. Ding, S.-C. S. Lin, B. Kiraly, H. Yue, S. Li, I.-K. Chiang, J. Shi, S. J. Benkovic, and T. J. Huang, "On-chip manipulation of single microparticles, cells, and organisms using surface acoustic waves," *Proceedings of the National Academy of Sciences*, vol. 109, no. 28, pp. 11 105–11 109, 2012.
[35] A. Riaud, J.-L. Thomas, E. Charron, A. Bussonnière, O. B. Matar, and M. Baudoin, "Anisotropic swirling surface acoustic waves from inverse filtering for on-chip generation of acoustic vortices," *Physical Review Applied*, vol. 4, no. 3, p. 034004, 2015.
[36] A. Riaud, M. Baudoin, O. B. Matar, L. Becerra, and J.-L. Thomas, "Selective manipulation of microscopic particles with precursor swirling rayleigh waves," *Physical Review Applied*, vol. 7, no. 2, p. 024007, 2017.
[37] M. Madadi, A. C. Jones, C. H. Arns, and M. A. Knackstedt, "3D imaging and simulation of elastic properties of porous materials," *Computing in Science & Engineering*, vol. 11, no. 4, p. 65, 2009.
[38] I. Sevostianov and M. Kachanov, "On approximate symmetries of the elastic properties and elliptic orthotropy," *International Journal of Engineering Science*, vol. 46, no. 3, pp. 211–223, 2008.
[39] A. J. Slobodnik Jr, E. D. Conway, and R. T. Delmonico, *Microwave Acoustics Handbook*. L. G. Hanscom Air Force Base, Bedford, MA USA: Air Force Cambridge Research Laboratories, 1970, vol. 1A, ch. Surface Wave Velocities.
[40] R. Weis and T. Gaylord, "Lithium niobate: summary of physical properties and crystal structure," *Applied Physics A*, vol. 37, no. 4, pp. 191–203, 1985.
[41] C. Campbell, *Surface acoustic wave devices for mobile and wireless communications*, ser. Applications of Modern Acoustics. New York, NY USA: Elsevier Science, 1998.
[42] L. Taupin, A. Lhémery, and G. Inquiété, "A detailed study of guided wave propagation in a viscoelastic multilayered anisotropic plate," in *Journal of Physics: Conference Series*, vol. 269, no. 1. IOP Publishing, 2011, p. 012002.
[43] K. Yamanouchi and K. Shibayama, "Propagation and amplification of Rayleigh waves and piezoelectric leaky surface waves in $LiNbO_3$," *Journal of Applied Physics*, vol. 43, no. 3, pp. 856–862, 1972.
[44] M. Munasinghe and G. Farnell, "Finite difference analysis of Rayleigh wave scattering at vertical discontinuities," *Journal of Geophysical Research*, vol. 78, no. 14, pp. 2454–2466, 1973.
[45] E. L. Adler, "Matrix methods applied to acoustic waves in multilayers," *IEEE Transactions on Ultrasonics, Ferroelectrics, and Frequency Control*, vol. 37, no. 6, pp. 485–490, 1990.

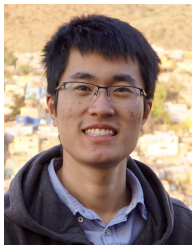

Naiqing Zhang received the B. Sc. degree in Department of Mechanics and Engineering Science at College of Engineering from Peking University, Beijing, China in 2016 and the M. Sc. degree in Department of Mechanical and Aerospace Engineering from University of California, San Diego, USA in 2017. He is currently pursuing the Ph.D. degree in Department of Mechanical and Aerospace Engineering from University of California, San Diego, USA. His research focuses on exploring phenomena of surface acoustic waves and developing acoustofluidics devices for small-scale fluid manipulation and biomedical applications.

Jiyang Mei holds the Bachelor's degree in Applied Physics from the University of Science and Technology of China. After attaining a M.S degree in Physics, he decided to switch the major to material science. He is now a graduate student, pursuing a Ph.D. degree in the Department of Materials Science and Engineering at University of California, San Diego, USA. He is currently working on surface acoustic wave devices with waveguide structures and its applications.

Tilvawala Gopesh holds Bachelor's and Masters degrees in Mechanical and Aerospace Engineering from Monash University, Melbourne, Australia. After his Masters degree, in pursuit of developing medical devices he moved to work under the guidance of Prof. James Friend. He is currently pursuing a PhD in the department of Mechanical and Aerospace Engineering at the University of California San Diego. His present research involves work on various medical devices ranging from effective pulmonary drug delivery, rapid diagnostics to soft robotic surgical devices for use in opthalmology and Neurosurgery.

James Friend James Friend is a Professor in the Center for Medical Devices and Instrumentation at the University of California, San Diego, leading the Medically Advanced Devices Laboratory. His research interests are principally in exploring and exploiting acoustic phenomena at small scales, mainly for biomedical applications. He currently supervises a team of seven PhD students and three post-docs. Over the years, he has over 260 peer-reviewed research publications (H-factor = 45) and 29 patents in process or granted, completed 33 postgraduate students and supervised 20 postdoctoral staff, and been awarded over $25 million in competitive grant-based research funding. He is a fellow of the IEEE and was awarded the IEEE Carl Hellmuth Hertz Ultrasonics Award from the IEEE in 2015.